JOURNAL OF GEOPHYSICAL RESEARCH, VOL. 106, NO. C12, PAGES 31,057–31,073, DECEMBER, 2001

Surface current variability east of Okinawa Island obtained from remotely sensed and in situ observational data

Yukiharu Hisaki

Department of Physics and Earth Sciences, Faculty of Science, University of the Ryukyus, Okinawa, Japan

Tsutomu Tokeshi and Wataru Fujiie

Interdisciplinary Graduate School of Engineering Sciences, Kyushu University, Fukuoka, Japan

Kenji Sato and Satoshi Fujii

Okinawa Radio Observatory, Communications Research Laboratory, Okinawa, Japan

Abstract. We investigated ocean surface current variability in the region east of Okinawa Island in the spring of 1998 using in situ and remotely sensed data including surface velocity estimates inferred from HF ocean radars. Most previous studies utilizing HF ocean radars were limited to shallow continental shelves. In contrast, most of the observation area in this study was in the open ocean. During the observation period the HF ocean radars sampled a region where anticyclonic and cyclonic mesoscale eddies were adjacent to each other. The HF-radar-derived ocean currents agree with those measured by a current meter. The surface currents were highly variable in both time and space and were affected by the eddy field in the offshore region. The current field was related to the near-surface water temperature. For example, a local temperature rise was often associated with northeastward flows. The surface currents in regions shallower than about 1000 m had a significant correlation with local wind forcing. Our HF ocean radars often detected a strongly convergent zone, which was different in character from those described in previous studies in that it was in the deep ocean. From other data such as National Oceanic and Atmospheric Administration advanced very high resolution radiometer imagery, we concluded that the convergent zone was due to mesoscale eddy fronts.

1. Introduction

Measurements of ocean surface currents are important for physical oceanography, fishery studies, and monitoring the coastal environment for contaminants such as oil pollution. One promising method that efficiently measures the evolving current field over broad spatial areas uses high-frequency (HF) ocean radars. HF ocean radars infer ocean surface currents and waves by analyzing the backscattered signals from HF radio waves, radiated over the ocean.

HF ocean radar systems have been developed in the United States to measure surface currents [e.g., *Barrick et al*., 1977] and ocean waves [e.g., *Barrick*, 1977]. In Japan they have been developed since 1988 by the Okinawa Radio Observatory, Communications Research Laboratory, for application to physical oceanography problems such as detecting "Kyucho" [*Takeoka et al*., 1995] and measuring ocean waves [*Hisaki*, 1996].

HF ocean radars are particularly useful for investigating currents associated with complex horizontal structures such as ocean fronts. However, the observation areas of most previous studies employing HF ocean radars were limited to shallow continental shelves because the observation range of shore-based 25-MHz HF ocean radars is limited to several tens of kilometers. (One of the few exceptions is the study by *Teague* [1986], who used a portable shipboard HF radar system.)

The region east of Okinawa (Ryukyu) Island is close to the Ryukyu trench, where water depth deepens rapidly with distance offshore. Therefore, even when shore-based HF ocean radars are used, most of the observation area can be characterized as open ocean rather than continental shelf.

Okinawa Island is located east of the main axis of the Kuroshio in the East China Sea. It is nevertheless important to investigate variabilities of spatial and temporal current fields in the region east of Okinawa Island in order to better understand the Kuroshio, because recirculation gyres and mesoscale eddies in the region affect its transport [e.g., *Yuan et al*., 1998; *Yang et al*., 1999]. For example, *Yuan et al*. [1998], on the basis of hydrographic data, showed that there are three branches of the Kuroshio east of Taiwan and that the easternmost branch flows past the region east of Okinawa Island. There have, however, been few studies of the temporal and spatial variability of this flow. One of the main objectives of this study was to describe the temporal and spatial variability of the current field east of Okinawa Island using HF ocean radars, other remotely sensed data, and in situ observations.

As mentioned later, we often observed a convergent zone within our observation area. Previous observations by HF ocean radars found that convergent zones were associated with fronts such as tidal fronts [*Matthews et al*., 1993] or a shelf slope front maintained by an incursion of open ocean water [*Marmorino et al*., 1998]. However, these examples do not apply to our case, because the detected convergent zone was in the deep ocean and not associated with the front between shelf and open-ocean waters. The other objective of our study was to investigate this open-ocean convergent zone.

Paper number 2000JC000784.
0148-0227/01/2000JC000784$09.00

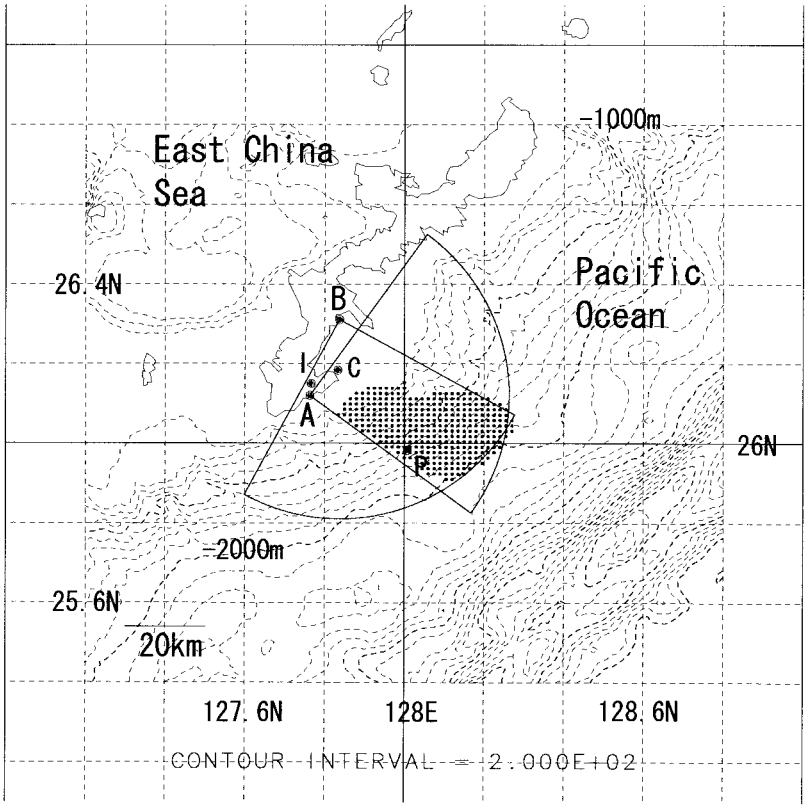

Figure 1. Map of the observation area. Letters A and B indicate locations of the HF ocean radars, C indicates tidal station, I indicates meteorological station, and P indicates current meter and temperature observation.

In section 2 we describe the principle of measuring ocean currents by HF ocean radar and the experimental design. Here we compare HF-ocean-radar-derived currents with in situ current data. Section 3 presents the general features of the surface variability; the results of temporal and correlation analyses are given in section 4. The convergent zone is described in section 5. Section 6 presents a discussion and draws conclusions.

2. Observation

2.1. Principles of Measuring Ocean Currents by HF Ocean Radars

A power spectrum as a function of Doppler frequency is obtained by radiating HF radio waves over an ocean area and performing a spectral analysis of the backscattered signals, which is called the Doppler spectrum. There are typically two prominent peaks in the Doppler spectrum, almost symmetric to each other with respect to zero Doppler frequency. These peaks are called first-order scattering. Ocean surface waves may be expressed as a superposition of linear waves as a first approximation. In the case of radio wave scattering, only the surface wave components whose wavelengths are half the radio wavelength and which propagate in the beam direction contribute to first-order backscattering. This is called Bragg scattering, and its Doppler frequency (Bragg frequency) is determined from the linear dispersion relationship of surface waves. However, in practice, the position of first-order scattering of the measured Doppler spectrum is somewhat different from the Bragg frequency. This difference is due to the advection of the surface waves by ocean currents. We can therefore estimate the radial component of the ocean current by estimating the frequency shift of the Bragg peaks. The HF ocean radars infer the current averaged over the top several tens of centimeters, because waves responsible for the backscattered energy have short horizontal wavelength. We get radial velocity estimates as a function of distance from the radar antenna by range gating, and we derive the two-dimensional velocity vector by measuring from two or more overlapping sites. Furthermore, there are secondary continuums around the first-order scattering. These are called second-order scattering and can be used to estimate ocean wave spectra [e.g., *Hisaki*, 1996]. The theoretical derivations of the Doppler spectrum are described in detail by *Hisaki* [1999] and *Hisaki and Tokuda* [2001].

2.2. Experimental Design and Data Analysis

The HF ocean radars of the Okinawa Radio Observatory, Communications Research Laboratory, were deployed along the east coast of Okinawa Island (Figure 1). The radars were located at site A (26°7.19′N, 127°45.78′E) and site B (26°18.63′N, 127°50.25′E) in Figure 1. Ocean current measurement by HF ocean radars was conducted from April 15, 1998, to May 15, 1998. The radio frequency was 24.5 MHz; the corresponding Bragg frequency was 0.505 Hz. The characteristics of the radar system are summarized in Table 1. The temporal resolution of the radar system is 2 hours, which is longer than that of the Ocean Surface Current Radar (OSCR) system [e.g., *Shay et al.*, 1995]. The beam forming is electronically controlled by the phase shifter in real time. The radar successively measures in one direction and then changes its direction for the next measurement. We used 12 beam direc-

Table 1. Characteristics of the HF Ocean Radar

Parameter	Value
Transmitter and receiver	
Center frequency	24.515 MHz
Transmitted power	100 W
Sweep bandwidth	100 kHz
Radar type	FMICW
Range resolution	1.5 km
Antenna	
Antenna type	ten-element phased array antenna
Aperture length	54.9 m
Beam width	15°
Beam directions	0 ± 45° (13 directions)
Polarization	vertical

tions in this study. The radar systems are available as 896 coherent I and Q signals at 0.5-s sampling intervals and are processed using a 256-point fast Fourier transform (FFT) after applying a Hamming window and overlapping by 50%. Therefore the radar data collection requires more than $0.5 \times 896 = 448$ s, and each measurement takes 10 min per direction. The radar gave us ocean surface current fields at 2-hour ($10 \times 12 = 120$ min) intervals. The radar observation time at site A was delayed 3 min relative to that at site B to avoid interference.

If we assume that radial velocities and errors are independent and RMS values of the errors of the radial velocities of two radars are equal, then the RMS error of the current vectors is amplified by a factor $1/|\sin(\Delta)|$, where Δ is the intersection angle between two radar beams [e.g., *Graber et al*., 1997]. We analyzed radar-estimated currents in the domain where the factor $1/|\sin(\Delta)|$ was less than 2.5. A map of this region is shown in Figure 1. The antenna aperture widths of more than 50 m restricted the areas where they could be deployed. Furthermore, there was an obstacle to radio wave transmission to the southeast and south of radar site A. Consequently, the radar at site A was steered too far to the north, leading to poor overlap with the coverage from the radar at site B, and thus limited observation. The measured currents were mapped to a grid with a horizontal resolution of 1.5 km, as shown in Figure 1. At almost all of the grid points, the water depth was greater than 200 m; at more than half of them it was greater than 1000 m.

In addition to the HF radar installation, a current meter and a temperature meter were deployed at location P (Payao, 25°59′N, 128°0.5′E) by the Okinawa Prefectural Fisheries Experiment Station. The current sensor, an Aanderaa RCM (recording current meter) 9, which is the Doppler current sensor (DCS), was deployed at 4 m depth. The DCS transmits acoustic waves to the side of the sensor, so the current sensor recorded ocean velocity at 4 m. The value of $1/|\sin(\Delta)|$ at Payao was 1.9. The current meter was deployed from March 3, 1998, to May 20, 1998. The sampling interval was 1 hour from 0700 LT March 3 to 0700 LT May 8, and 2 hours from 0800 LT May 8 to May 20.

Hourly surface wind data at location I (Itokazu, 26°09′N, 127°46′E) were supplied by the Japan Meteorological Agency (JMA). The resolution of the wind speed was 1 m s^{-1}, and the resolution of the wind direction was 22.5° (16 directions). To investigate the horizontal variations of the wind field, we used wind data at South Daito Island (25°49.7′N, 131°13.5′E), also supplied by the JMA. Hourly sea level data at location C (Chinen, 26°11′N, 127°50′E) were supplied by the Geographical Survey Institute.

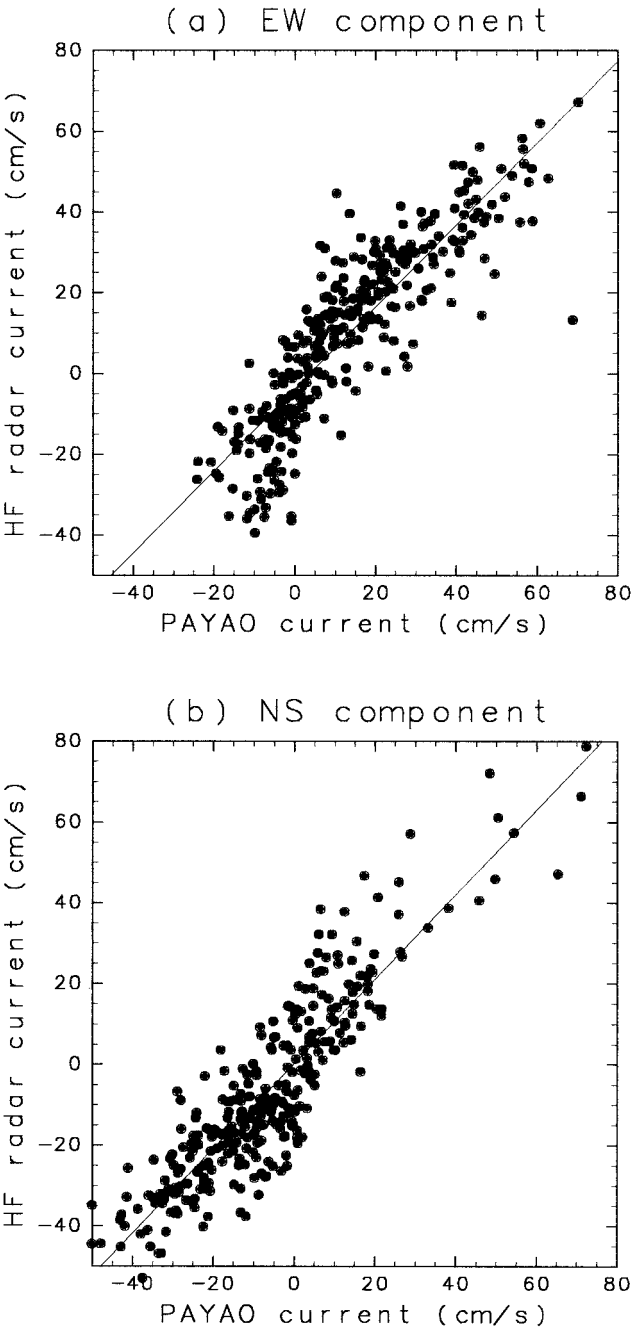

Figure 2. Scatter diagrams between currents measured by the current meter and HF ocean radars. (a) EW components. (b) NS components.

In addition to the HF ocean radar and in situ data, we used National Oceanic and Atmospheric Administration (NOAA) advanced very high resolution radiometer (AVHRR) imagery and altimetric data from the TOPEX/Poseidon (T/P) satellite. The NOAA/AVHRR imagery data (channel 4) provide sea surface temperature (SST) data, and the altimetric data from T/P indicate geostrophic current anomalies. Unfortunately, most of the NOAA/AVHRR imagery data were taken under cloudy conditions. We therefore used daily-averaged SST data from the Tropical Rainfall Measurement Mission (TRMM) Microwave Imager (TMI). The spatial resolution of SST from the TMI was 0.25° × 0.25°. The radio frequency of TMI was

Table 2. Comparison Between HF-Ocean-Radar-Derived Currents and Current-Meter-Measured Currents at Payao[a]

	$u_P - u_r$	$v_P - v_r$
Correlation	0.87	0.89
RMS difference, cm s^{-1}	11.68	10.47
Slope	1.015	1.047
Bias, cm s^{-1}	−3.89	0.043

[a]Here u_r is the east-west component, v_r is the north-south component, and u_P is the east-west component, v_P is the north-south component.

Table 3. Comparison Between Sea Surface Temperature From TMI (T_m) and Buoy-Measured Temperatures (T_b)

	$T_b - T_m$
Correlation	0.977
RMS difference, deg	0.804
Slope	1.00
Bias, deg	−0.192

10.7 GHz [e.g., *Shibata et al*., 1999]. Although the spatial resolution of TMI SST data is much larger than that of the NOAA/AVHRR SST data and we could not estimate SST from TMI near the coast, the advantage of the TMI SST is that it had less degradation from clouds than the NOAA/AVHRR SST data. The algorithm for estimating SST from TMI is described by *Shibata et al*. [1999].

2.3. Comparison of Remotely Sensed Data and in Situ Observations

2.3.1. Comparison of currents. We compared HF-ocean-radar-derived currents with currents measured by the current meter at location Payao. We estimated HF-ocean-radar-derived currents at Payao by linear interpolation in space. Figure 2 shows scatter diagrams between the currents measured by the current meter and by the HF ocean radars for the east-west (EW) and north-south (NS) components. The number of samples in the comparison was 309. The study finds good agreement; results are summarized in Table 2. The correlations are greater than 0.85, and the RMS difference between the sensors is about 11 cm s^{-1}. The differences between the radar-derived currents and in situ data in the region (grid points in Figure 1) are at most about 14 cm s^{-1}.

The slopes and biases of the regression lines to the scatterplots are about 1 and −4 cm s^{-1}, respectively. The bias of EW components is significant at the 99% confidence level. These values are comparable with those in previous studies [e.g., *Shay et al*., 1995; *Paduan and Rosenfeld*, 1996; *Graber et al*., 1997; *Chapman et al*., 1997]. Part of the discrepancy may be due to the different depth of the two measurements. Furthermore, the HF-ocean-radar-derived currents were weight-averaged values of the currents in the radar-illuminated cell. On the other hand, the current meter measured at one point. Considering the difference in data sampling methods, we concluded that the errors in the HF-radar-derived currents were actually smaller than the sensor discrepancy estimates given here.

2.3.2. Comparison of SST. The accuracy of the TMI SST data is not as well established as that of the NOAA/AVHRR SST data. We compared TMI SST data with the buoy-measured daily-averaged water temperature at 29.0°N and 135.0°E. The period of the comparison was 1 year (1998). Figure 3 is a scatter diagram between buoy-measured temperature and SST from TMI. The number of samples for the comparison was 353. We find good agreement; the comparison is summarized in Table 3. The correlation is about 0.98, and the RMS difference between them is about 0.8°C. From this analysis we conclude that SST from the TMI is sufficiently accurate for our purposes.

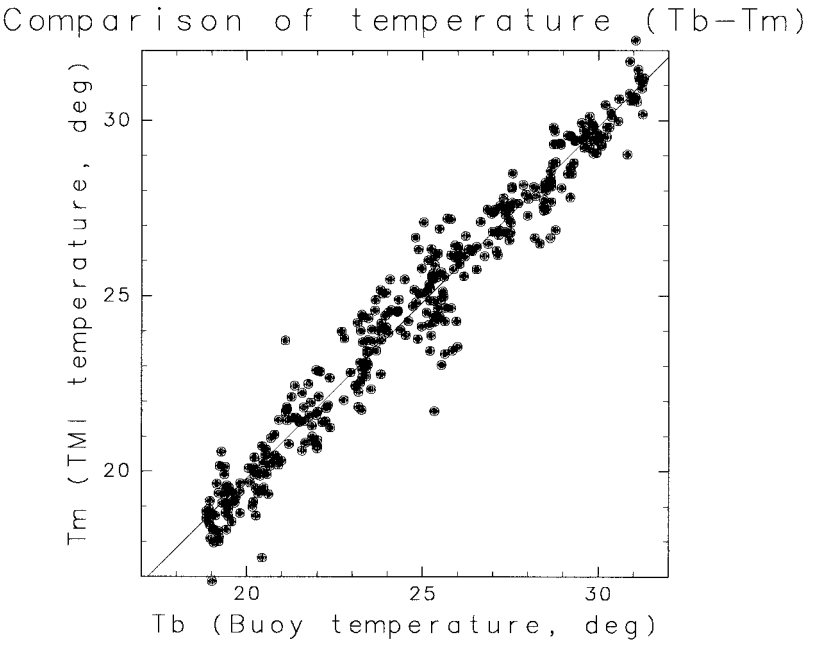

Figure 3. Scatter diagrams between buoy-measured temperatures and sea surface temperature (SST) from Tropical Rainfall Measurement Mission (TRMM) Microwave Imager (TMI).

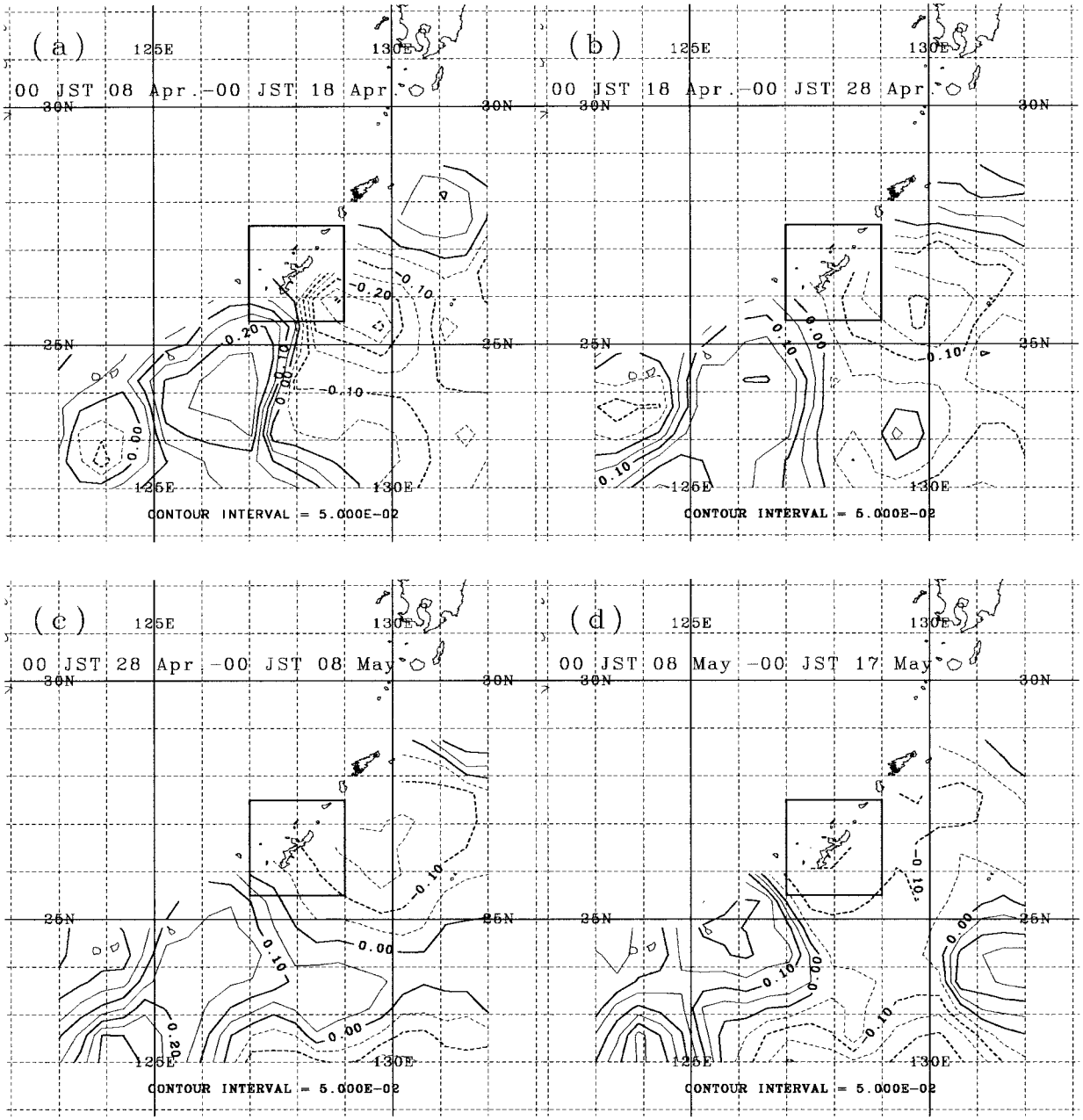

Figure 4. Maps of spatial distributions of the residual sea surface height (RSSH) during the HF ocean radar observation period: (a) from 0000 LT April 8 to 0000 LT April 18, 1998. (b) from 0000 LT April 18 to 0000 LT April 28, 1998, (c) from 0000 LT April 28 to 0000 LT May 8, 1998, and (d) from 0000 LT May 8 to 0000 LT May 17, 1998. Units are meters, and the contour interval is 0.05 m. The box in each panel (127°E–129°E and 25.5°N–27.5°N) outlines the area of Figure 1 for reference.

3. Spatial Variability

3.1. Sea Surface Height Anomaly

Residual sea surface heights (RSSH) from T/P altimetric data were estimated by removing the time-mean surface and Geoid heights, tidal height signals, and the effects of the inverse barometer. The mean sea surface was computed using GEOS 3, Seasat, Geosat, and about 15 months (from November 1992 to February 1994) of T/P altimetric data [*Benada*, 1997]. The RSSH is thus the time anomaly of the surface pressure field and can be used to infer geostrophic current anomalies with respect to the mean geostrophic current.

Since the temporal and spatial resolutions of the T/P altimetric data are much coarser than those of the HF ocean radar currents, it is not feasible to quantitatively relate detailed structures seen by the HF-ocean-radar-derived currents with T/P RSSH fields. However, it is useful to document the general RSSH features to help interpret the current fields from the HF ocean radars.

Figure 4 presents maps of RSSH in the region east of Okinawa Island during the observation period of the HF ocean radars. Both cyclonic and anticyclonic eddies are seen in the vicinity of the radar observation range. Note, for example, a cyclonic eddy centered at 25.5°N, 129.5°E and an anticyclonic

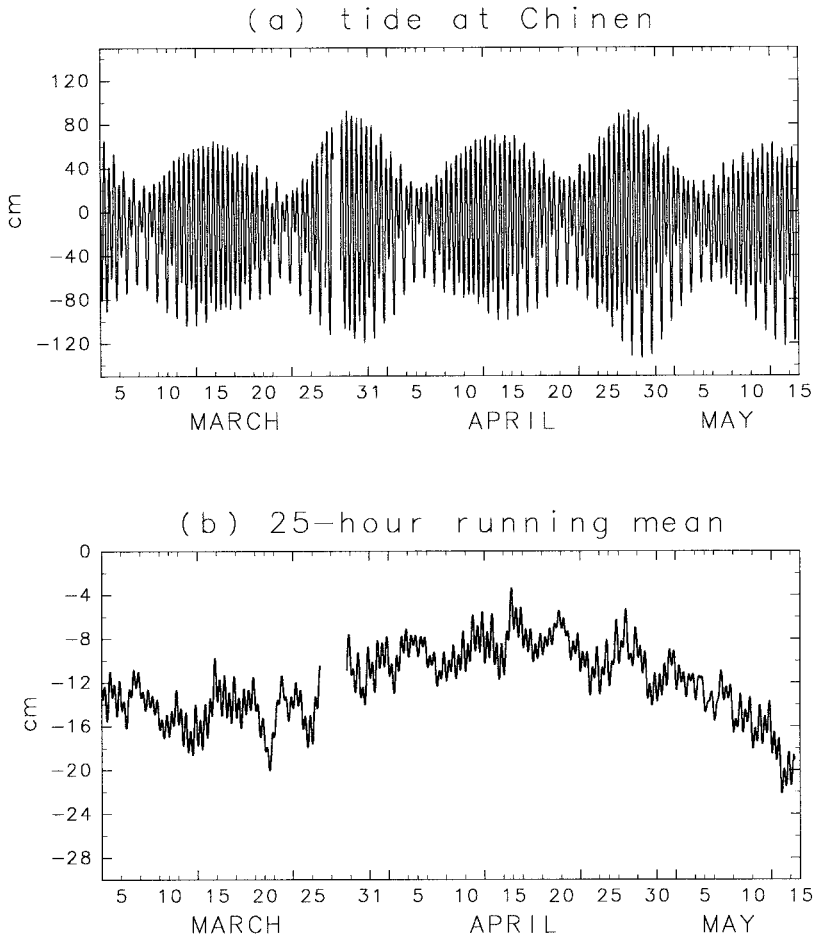

Figure 5. (a) Time series of sea levels at Chinen. (b) Time series of 25-hour running mean sea levels at Chinen (letter C in Figure 1).

eddy at 24°N, 126.5°E in Figure 4a. The radar observation area was between these eddies at this time. The geostrophic current anomaly inferred from the RSSH estimates was southward in the first quarter of the study period (Figure 4a), whereupon the current anomaly turned eastward in the next two quarters (Figures 4b and 4c). By the end of the observation period, the current anomaly was almost northeastward (Figure 4d).

Figure 5a is a time series of sea level at Chinen, with Figure 5b showing a 25-hour running mean of these data. Since we could not obtain tide gauge data during the periods 0800–1100 LT March 26, 1998, 0900 LT March 27, 1998, to 0200 LT March 28, 1998, and 2300 LT May 14, 1998, to 0900 LT May 18, 1998, we used a simple box filter to suppress the tidal signals. The low-passed sea level at Chinen was maximum in mid-April and then fell through the remainder of the observation period, which is consistent with altimetric data in Figure 4.

3.2. Mean Current Fields During the Observation Period

Figure 6a presents the mean surface current fields over the 29-day interval observed by the HF ocean radars. The currents near the coast were generally weak and directed northeastward. Southward mean flow was observed off the coast of Okinawa Island. In contrast, the mean wind at Itokazu (also indicated) was northwestward. Our observations seem to be consistent with those of *Yuan et al*. [1998], who documented a branch of the Kuroshio flowing to the northeast near the coast of Okinawa Island with southward flow farther off the coast. However, our observed current fields were variable. Southward or southeastward flows were dominant until the third quarter of the observation period (Figures 6b–6d), whereas northeastward flows were dominant in the last quarter (Figure 6e), except in the offshore area.

If we assume that the mean geostrophic currents were weak compared with geostrophic current anomalies, these flow patterns are consistent with the altimetric data in Figure 4, as explained in section 3.1. In fact, as shown in Figure 8, later, the currents changed direction markedly in time and the mean current was indeed smaller than the current anomalies. The synoptic current field in the region east of Okinawa Island is due chiefly to the eddy field in the region.

3.3. SST Fields From TMI

Figure 7 shows the mean SST field during the HF radar observation period. The strong temperature gradient visible west of Okinawa Island (East China Sea) indicates the main axis of the Kuroshio. Isotherms in the vicinity of the HF ocean radar observation area (around 26°N, 128°E) were oriented north-south or northwest-southeast, which suggests southward or southeastward currents. This is consistent with Figure 6. Furthermore, a temperature front near the HF ocean radar observation area seen in the first quarter of the observation period (Figure 7b) appears consistent with the altimetric data (Figure 4a).

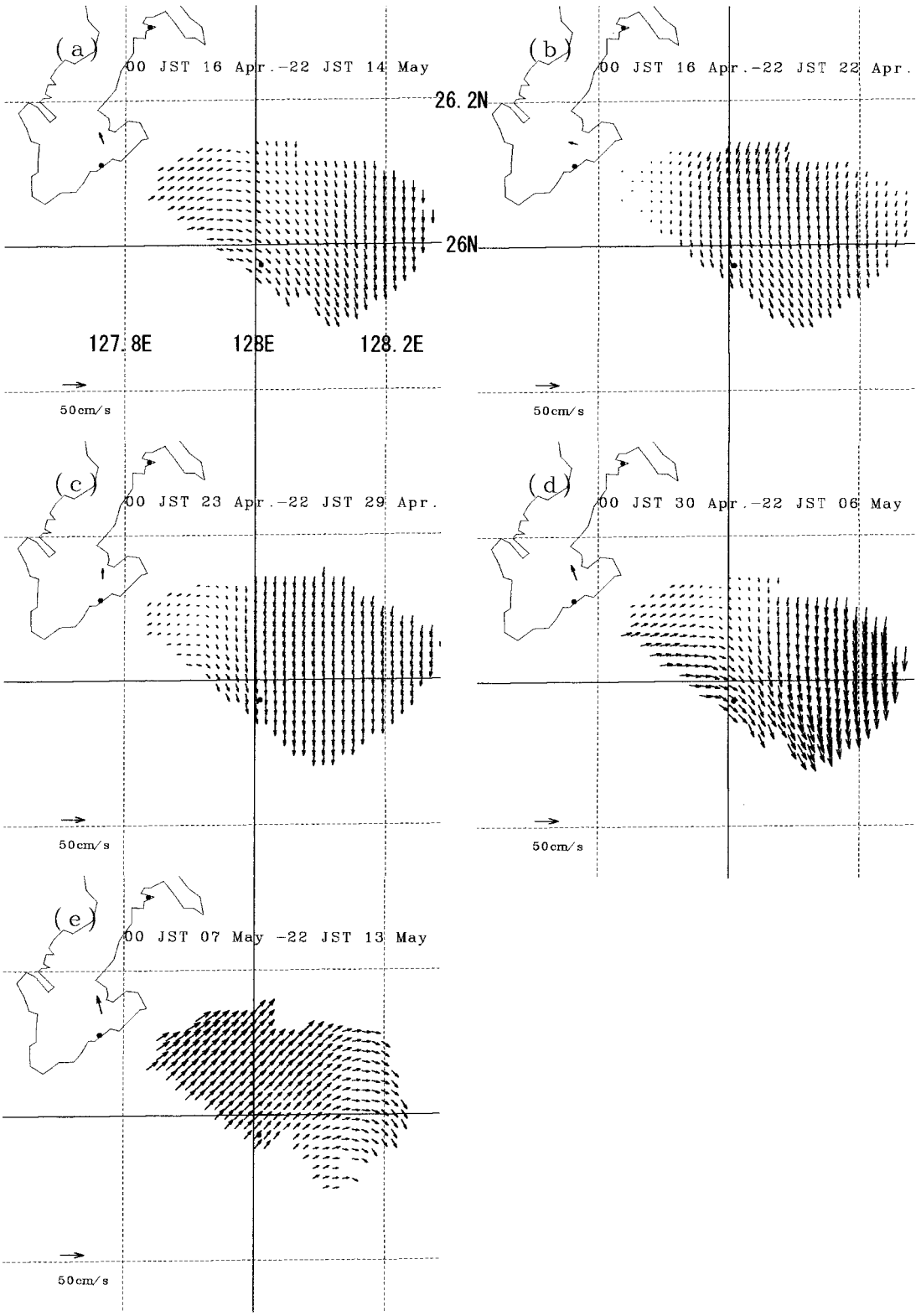

Figure 6. Mean surface current fields observed by HF ocean radars. The averaged periods are (a) from April 16 to May 14, 1998, (b) from April 16 to April 22, 1998, (c) from April 23 to April 29, 1998, (d) from April 30 to May 6, 1998, and (e) from May 7 to May 13, 1998. The arrow at I (Figure 1) is the mean wind vector during the period (10% of the magnitude).

4. Temporal Variability

4.1. Time Series and Correlation Analysis

Figure 8 shows time series of EW and NS components of ocean currents and temperatures measured at Payao. Several abrupt temperature rises were observed, for example, on March 31, April 10 (particularly notable), April 23, and May 2. The EW component of surface current (Figure 8a) became larger during the period. The temperature rises were associ-

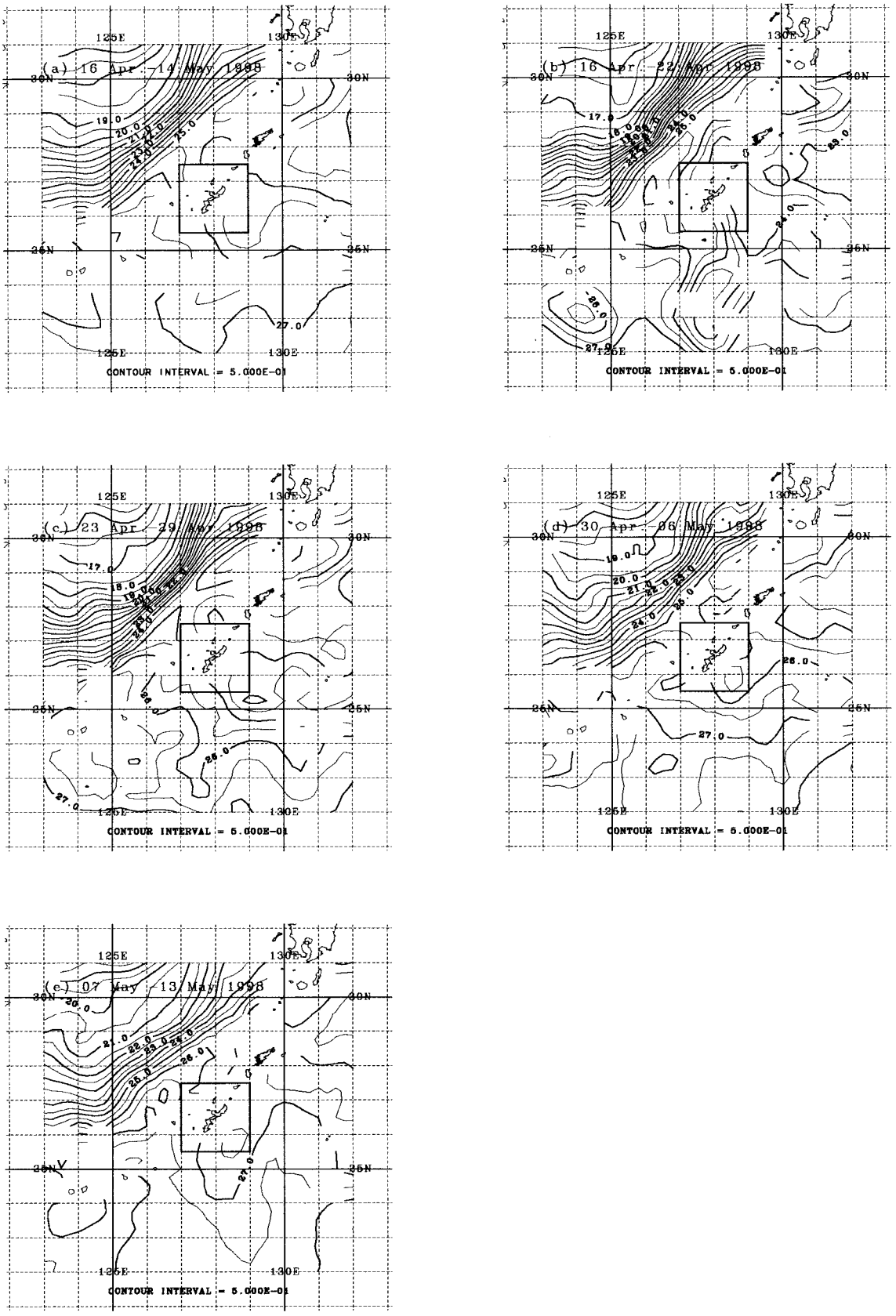

Figure 7. Mean SST from TMI. The averaged periods were (a) from April 16 to May 14, 1998, (b) from April 16 to April 22, 1998, (c) from April 23 to April 29, 1998, (d) from April 30 to May 6, 1998, and (e) from May 7 to May 13, 1998. Units degrees, contour interval is 0.5°. The box in each panel (127°E–129°E and 25.5°N–27.5°N) outlines the area of Figure 1 for reference.

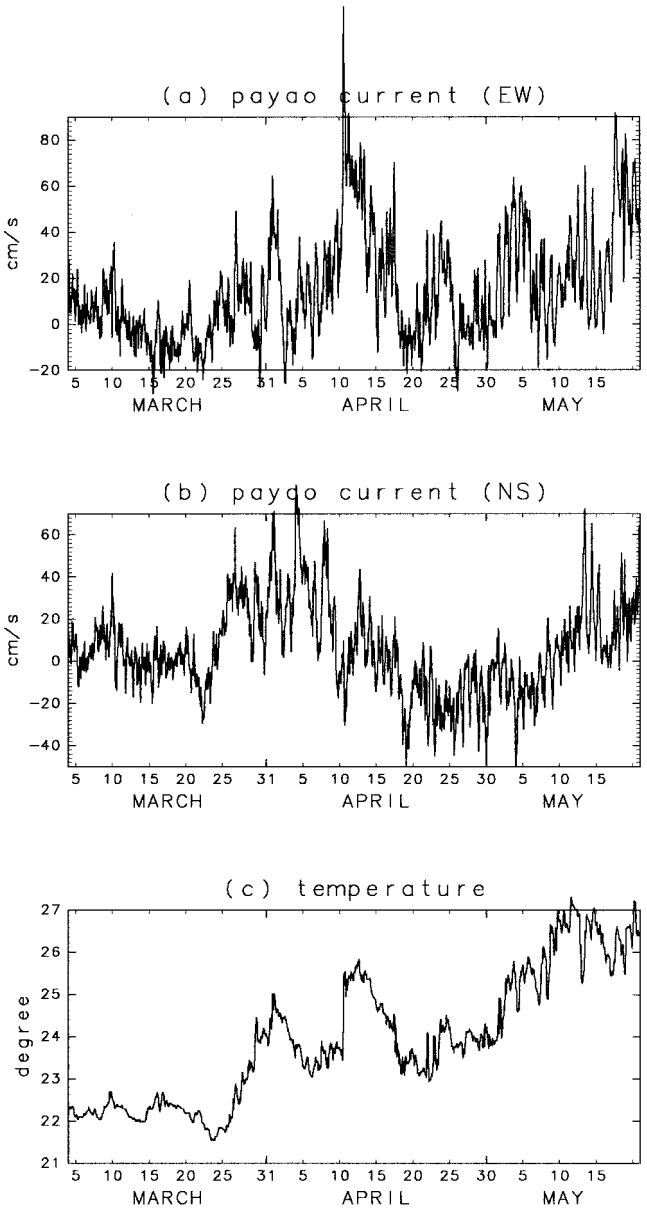

Figure 8. Time series of (a) EW and (b) NS components of ocean currents and (c) temperatures measured at Payao (letter P in Figure 1).

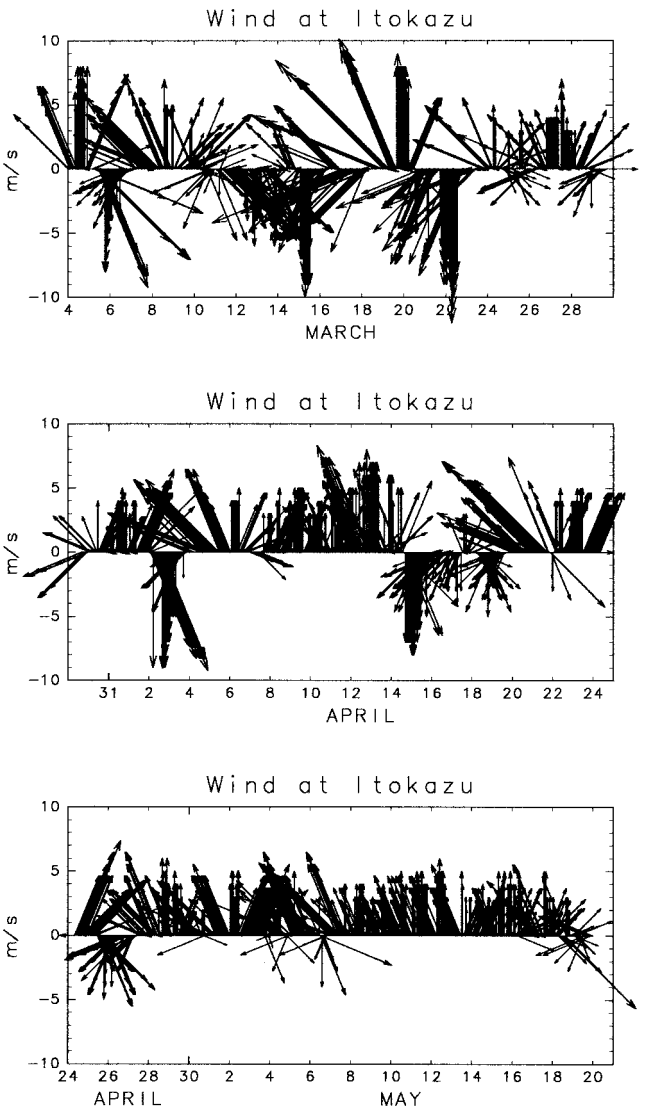

Figure 9. Time series of winds at Itokazu (letter I in Figure 1).

ated with enhanced eastward flows. The NS component of current at Payao was negative (southward) after April 15 (observation period by HF ocean radar), as shown in Figures 6a and 8b. However, the flow was northward before April 14, as shown in Figure 8b. The average values of the EW and NS components from March 3 to May 20 are 15.1 and 5.5 cm s^{-1}, respectively. The standard deviations of the EW and NS components are 23.2 and 21.2 cm s^{-1}, respectively, which are larger than the mean values. Figure 9 shows time series of winds at Itokazu. The wind directions were highly variable in March, while they were consistently northward or northwestward during the HF radar observation period, except in mid-April. We see no clear relationship between the abrupt temperature rises (Figure 8c) and the winds. To investigate the relationship between currents and temperatures, we calculated the correlations between current components and temperature anomalies for daily-averaged data. The temperature anomalies were those from a linear trend in time. Figure 10a shows the correlations as a function of direction. Figure 10b is a scatter diagram of the direction in which the correlation takes a maximum value. The current component in a direction means the projection of the current vector in that direction. For example, the value for 90° (horizontal axis) in Figure 10a means a correlation between the NS component of currents and temperature anomalies. The maximum correlation is 0.59, at a direction of 44°. This indicates that temperature rises were associated with northeastward flow. We also calculated the correlations between wind components at Itokazu and temperature anomalies at Payao for daily-averaged data (Figures 10c and 10d). There was no significant correlation between them.

Figure 11 shows maps of the complex correlations between daily-averaged wind vectors and daily-averaged ocean currents derived from HF ocean radars. The averaged wind vectors and ocean currents are expressed as $U_w = u_w + iv_w$ and $U_r = u_r + iv_r$, where u_w and v_w are the east-west and north-south components of daily-averaged wind vectors, respectively; u_r and v_r are the east-west and north-south components of daily-

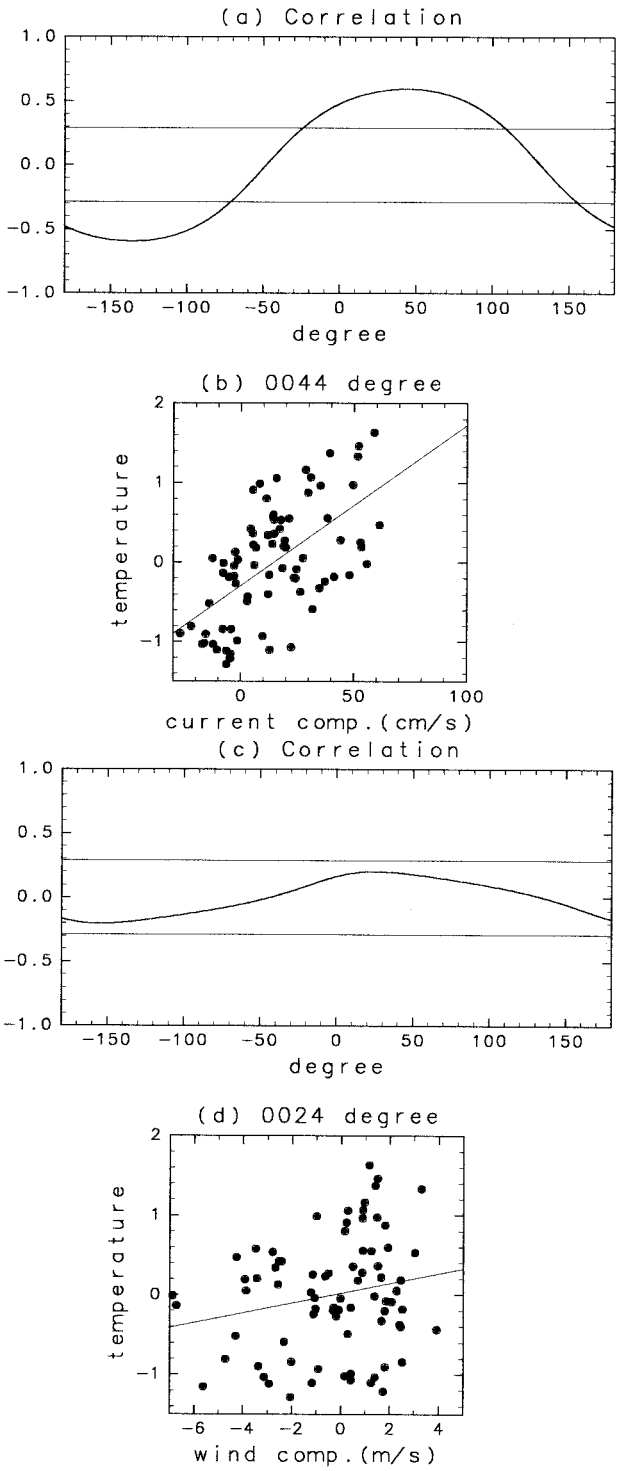

Figure 10. (a) Correlations as a function of direction between daily-averaged current components in a direction with respect to the eastward direction (counterclockwise is positive) and daily-averaged Payao temperature anomalies. The line (±0.289) indicates a significant correlation value for the 99% confidence level (the degrees of freedom is 76). (b) Scatter diagram in the direction in which the correlation takes a maximum value. (c) Same as Figure 10a but for daily-averaged wind components at Itokazu. (d) Same as Figure 10b but for daily-averaged wind components at Itokazu.

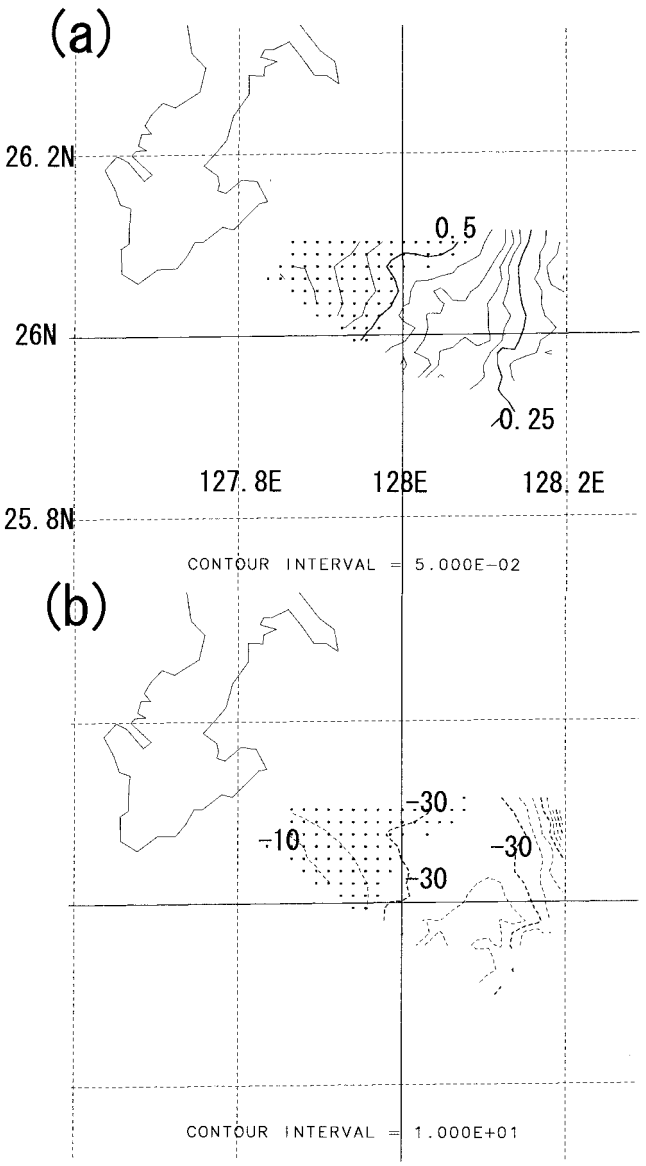

Figure 11. Maps of complex correlation between daily-averaged wind vectors at Itokazu (letter I in Figure 1) and daily-averaged ocean currents: (a) absolute value of the complex correlation and (b) argument of the complex correlation. Units are degrees. The significant correlation points for the 99% confidence level are indicated as grid points (the degrees of freedom is 27).

averaged surface currents, respectively; and $i = (-1)^{1/2}$. We calculated a complex correlation r_w as

$$r_w = \frac{\langle (U_w - \langle U_w \rangle)^* (U_r - \langle U_r \rangle) \rangle}{\langle |U_w - \langle Uw \rangle|^2 \rangle^{1/2} \langle |U_r - \langle U_r \rangle|^2 \rangle^{1/2}}, \quad (1)$$

where the asterisk means complex conjugate and angle brackets indicate the time average. The direction of the wind-driven current with respect to the wind direction is related to the argument of the complex correlation r_w.

Significant correlation between winds and currents (99% confidence level) is limited to the coastal area where the water depth is less than 1000 m (Figure 11a). The degrees of freedom is 27. The arguments of the complex correlations r_w in the region where the correlations are significant are negative, rang-

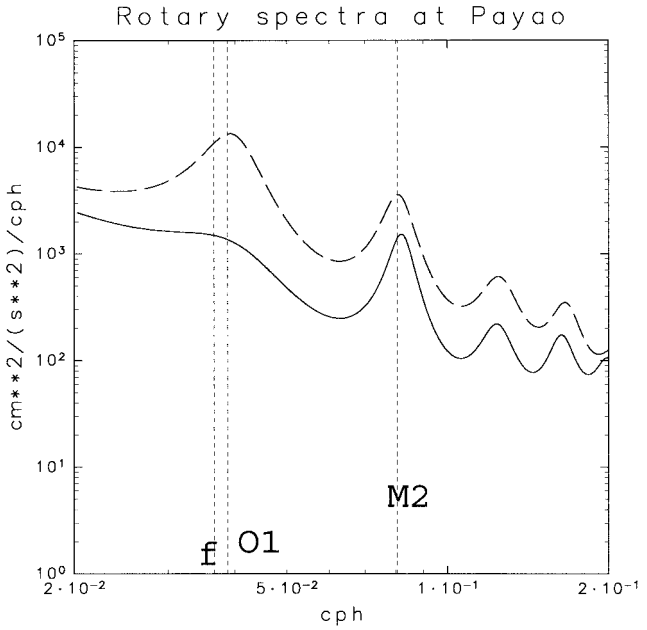

Figure 12. Rotary spectrum of ocean currents measured by current meter at Payao estimated by maximum entropy method (MEM). Solid line indicates counterclockwise, dashed line indicates clockwise; f is inertial frequency (1/27.4 cph).

ing from about −30° to −10°. This shows that the wind-driven currents are directed slightly to the right of the wind directions, which is qualitatively consistent with the Ekman theory, although the angle is smaller than 45°.

We do not have wind data from an ocean buoy in our study region. Therefore, to investigate horizontal variations in wind fields, we calculated the complex correlation r_w of daily-averaged winds between Itokazu (26°09′N, 127°46′E) and South Daito Island (25°49.7′N, 131°13.5′E) from April 16 to May 14, 1998. The absolute value of the complex correlation r_w between the two wind stations is 0.778, and the argument is 27.3°. This value ($|r_w| = 0.778$) is higher than the correlation between winds at Itokazu and HF-radar-derived ocean currents. While there can be differences between winds over land and water, this correlation analysis suggests the winds have large spatial scale. Therefore we incorporated land-based wind data in our study of offshore currents. Our explanation for decreased correlation between winds and HF-radar-derived currents in the offshore region is because of an increased influence of mesoscale eddies. The winds affected surface currents in the continental region shallower than about 1000 m. Winds probably also affect deep ocean surface currents as much as coastal waters. However, eddies add uncorrelated velocity structures, particularly in the region where the water is deeper than 1000 m.

Furthermore, horizontal gradients of the quasi-geostrophic flow in the background can affect the relationship between winds and surface currents. For example, *Weller et al.* [1991] discussed the relationship based on the equations as

$$\frac{\partial u_m}{\partial t} + 2u_m\frac{\partial u_q}{\partial x} + u_m\frac{\partial v_q}{\partial y} + v_m\left(\frac{\partial u_q}{\partial y} - f\right) = \frac{\tau_x}{\rho H} - cu_m \quad (2)$$

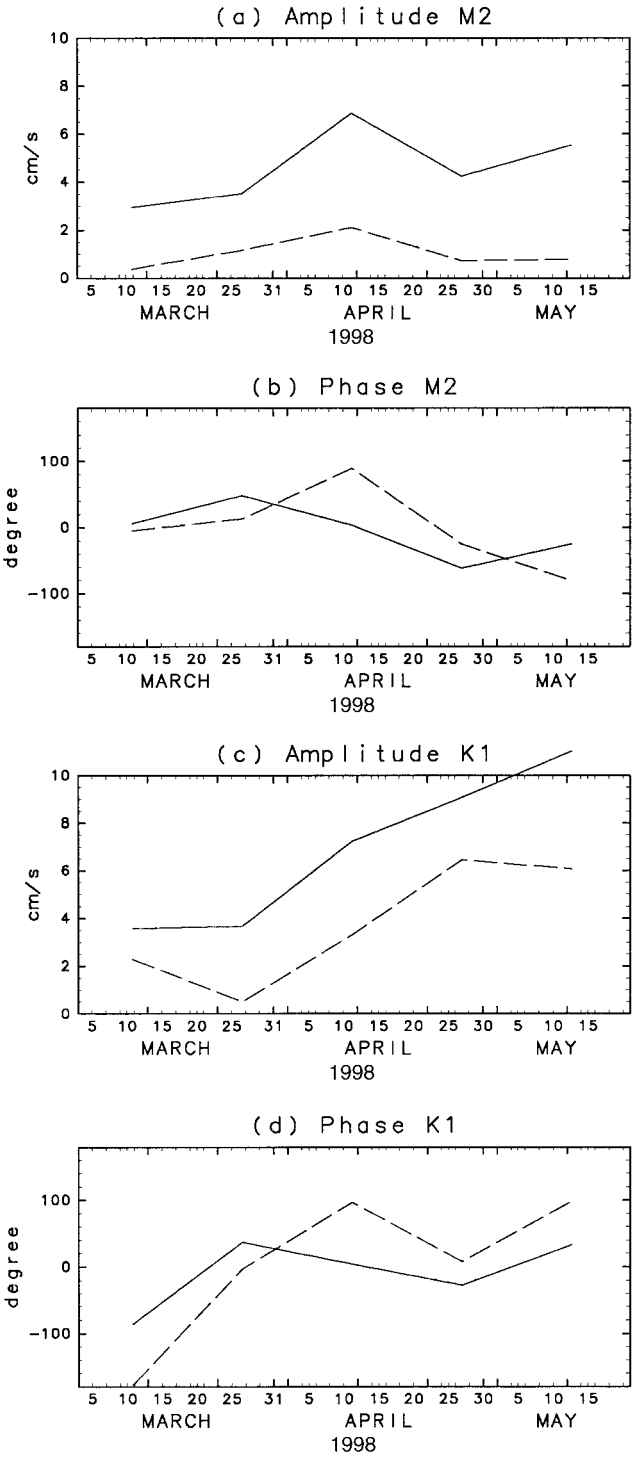

Figure 13. Tidal components for tidal ellipses of the M_2 and K_1 constituents. (a) Solid line, length of the major axis for M_2 tide; dashed line, length of the semimajor axis for M_2 tide. (b) Solid line, direction of the major axis with respect to the eastward direction (counterclockwise is positive) for M_2 tide; dashed line, direction of the tidal components at the reference time (0000 LT March 1, 1998) with respect to the major axis (clockwise is positive). (c) Same as Figure 13a for K_1 tide. (d) Same as Figure 13b for K_1 tide.

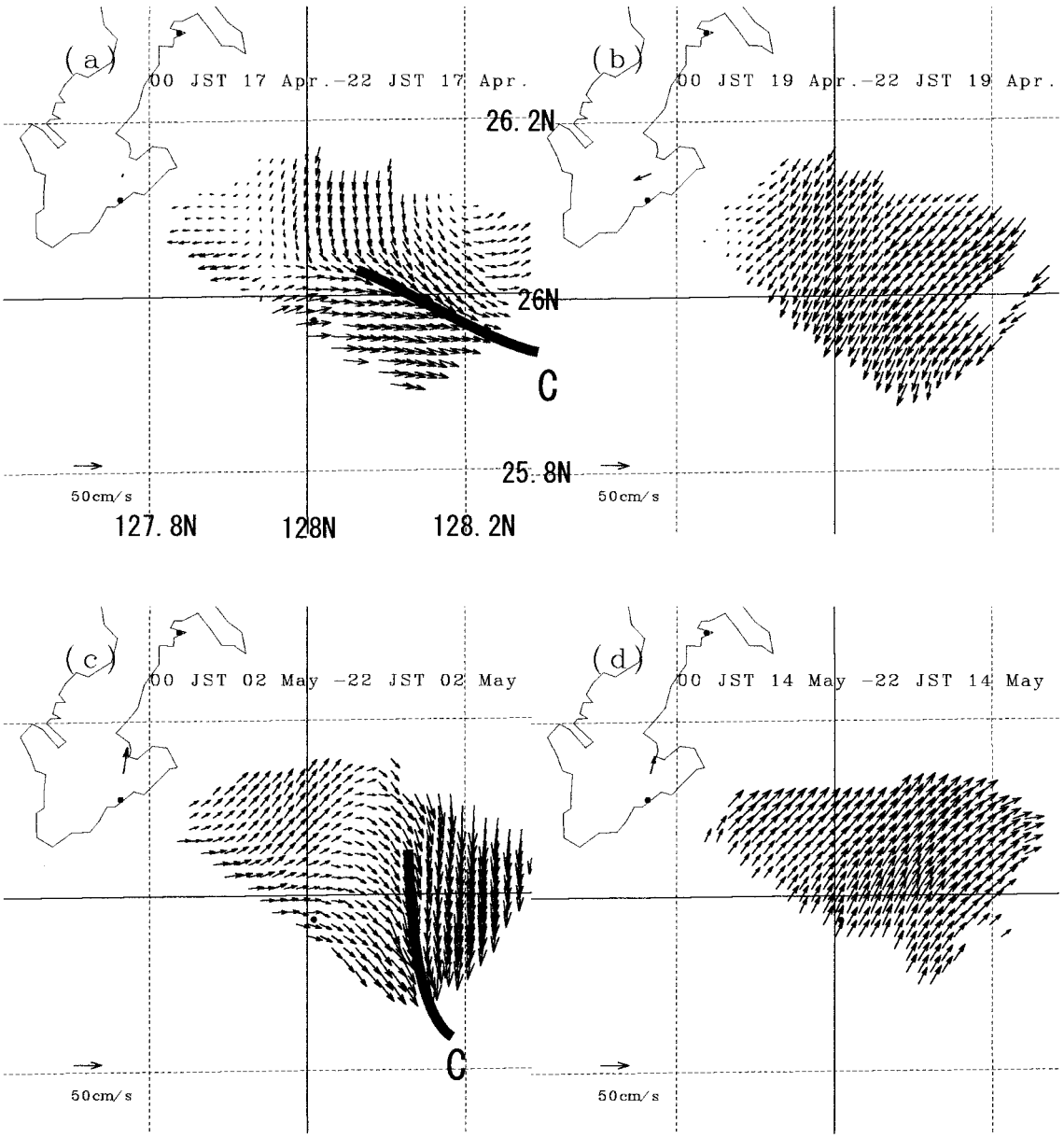

Figure 14. Examples of daily-averaged surface current: (a) April 17, 1998, (b) April 19, 1998, (c) May 2, 1998, and (d) May 14, 1998.

$$\frac{\partial v_m}{\partial t} + 2v_m\frac{\partial u_q}{\partial x} + v_m\frac{\partial v_q}{\partial y} + u_m\left(\frac{\partial v_q}{\partial x} + f\right) = \frac{\tau_y}{\rho H} - c\,v_m, \tag{3}$$

where t is the time, (x, y) are the horizontal coordinates, $\mathbf{u}_q = (u_q, v_q)$ are quasi-geostrophic flows, (u_m, v_m) are mixed-layer velocities, H is the depth of the mixed layer of density ρ, (τ_x, τ_y) are the components of the wind stress vector, and c is a damping coefficient. *Weller et al.* [1991] concluded that near-inertial oscillations are damped (amplified) with time when quasi-geostrophic currents are divergent (convergent), if both the divergence and relative vorticity of the quasi-geostrophic flow are small compared with the Coriolis parameter f and if the vertical gradient of the vertical component of the quasi-geostrophic flow is small compared with horizontal gradients of (u_q, v_q). However, we cannot see a clear relationship between the magnitudes of the wind-current correlations (Figure 11) and the patterns of surface currents (Figure 6). The spatial variability of the local wind-driven flows and the near-inertial response should be investigated quantitatively based on (2) and (3).

4.2. Spectral and Tidal Analysis

Figure 12 shows the rotary spectrum of ocean currents measured by the current meter at Payao. To distinguish diurnal tides from inertial oscillations, we used the maximum entropy method (MEM) (and the Burg method) spectral analysis technique. In fact, we also calculated a rotary spectrum by fast Fourier transform (FFT), but we could not distinguish inertial oscillations from the diurnal tide. The data during the period from 1400 LT March 3 to 0700 LT May 8, 1998, were used for the spectral analysis, because there were no missing data during this period. Diurnal tides (O_1) were more dominant than semidiurnal tides (M_2) at the location; inertial oscillations are

not evident during the period (Figure 12). To investigate the stationarity of the amplitudes and phase of the tidal currents, we divided the observation period at Payao (from 0700 LT March 3 to 2200 LT May 20, 1998) into five subintervals. The first period was from 0700 LT March 3 to 0000 LT March 19, the second was from 0000 LT March 19 to 1700 LT April 3, the third was from 1700 LT April 3 to 1000 LT April 19, the fourth was from 1000 LT April 19 to 0300 LT May 5, and the last was from 0300 LT May 5 to 2000 LT May 20. We conducted a harmonic analysis for four main tidal components (K_1, O_1, M_2, S_2) in each period. Figure 13 shows the tidal components for tidal ellipses of the M_2 and K_1 constituents. The amplitude and phase of the tidal components were variable. This suggests that internal tides were dominant in the region. In fact, the inertial frequency at the latitude (26°N) is lower than diurnal tidal frequencies (Figure 12), and both M_2 and K_1 tidal-period fluctuations can propagate as internal waves. However, since we have data only near the sea surface, and we do not have vertical profiles of currents and water densities, our information on internal tides is limited and we are unable to investigate internal tides further.

5. Convergent Zone

5.1. Appearance of the Convergence Region

Figure 14 shows the daily-averaged current fields observed by the HF ocean radars. We calculated daily-averaged currents for grid points where 2-hourly data were available at least 75% of the time (9–12 samples per day).

As indicated by curve C in Figures 14a and 14c, prominent convergent zones were observed off Okinawa Island. For example, the southeastward and southwestward flows form a convergent zone in Figure 14c. The water depth of the convergent zone is greater than 1000 m. The convergent zone often appeared in the region, for example, on April 16, April 22, April 29, May 2, and May 5.

Convergent zones have often been observed with HF ocean radars associated with fronts [e.g., *Matthews et al*., 1993; *Shay et al*., 1998; *Marmorino et al*., 1998]. However, the observation areas of these studies were limited to shallow continental shelves and at shelf breaks. In these cases the convergent zones were maintained by open-ocean water intruding onto the continental shelf. Our convergent zones were apparently of a type different from those in previous studies, because they were detected in the open ocean.

The location of the convergent zone was variable and was not always detectable. For example, in Figure 14b, the current field is almost unidirectional (directed southwestward) and no front was seen. It may be that the front existed south of the HF ocean radar observation area at this time. Another example is shown in Figure 14d, where the current field is nearly everywhere northeastward.

Figure 15 shows the mean, standard deviations, and maximum values of the convergence ($-\nabla_H \cdot \mathbf{v}_r$, $\mathbf{v}_r$: current vector) for daily-averaged data and their positions (latitude and longitude). We used a two-grid-point centered difference to compute convergence from the HF radar data. If we assume that the error of the current components is 15 cm s^{-1}, the error level of the convergence for daily-averaged currents is $\sqrt{(1/3)^2 \times 4} \times 15/\sqrt{12} \simeq 2.9$ ($\times 10^{-5}$ s^{-1}). The error of the current components is smaller than 15 cm s^{-1}, as described in section 2.3.1, so the error level of the convergence is smaller than 2.9×10^{-5} s^{-1}. We see strong convergences on April 17 and May 2, with values of 10×10^{-5} s^{-1}. The positions of the maximum convergence on April 17 and May 2 are close to curve C in Figures 14a and 14c. The maximum values of the convergence were small on April 19 and May 14, as shown in Figures 14b and 14d.

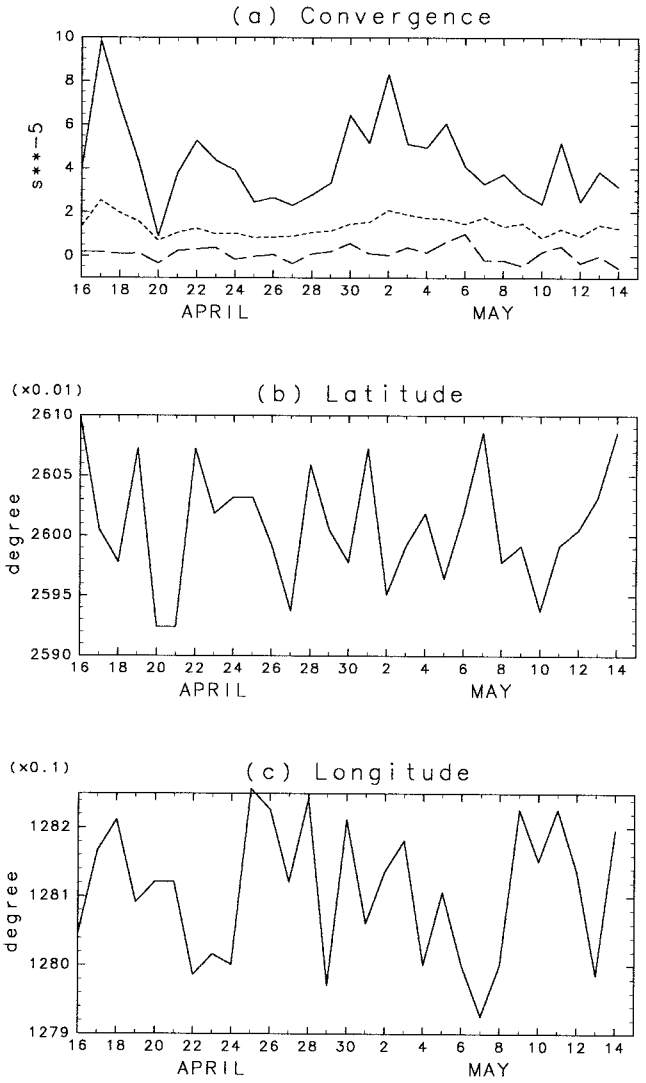

Figure 15. (a) Mean (dashed line), standard deviation (dotted line), and maximum value (solid line) of the convergence ($-\nabla_H \cdot \mathbf{v}_r$, $\mathbf{v}_r$: current vector) for daily-averaged current data in the region in Figure 1. Also shown are (b) latitude and (c) longitude, of the maximum convergence.

5.2. Comparison With Other Remotely Sensed and in Situ Data

5.2.1. NOAA/AVHRR imagery data. Although most of the NOAA/AVHRR imagery were obscured by clouds, a few examples were less degraded. Plate 1 shows examples of NOAA/AVHRR imagery data (channel 4), along with the 24-hour averaged current vector maps around the time of the images. For example, Plate 1a is the averaged current vector map from 1400 LT April 16 to 1200 LT April 17, 1998, with the NOAA/AVHRR image from 0300 LT April 17, 1998. A strong convergent zone is seen around curve Ca in Plate 1a where southeastward flow encountered an eastward flow. Interestingly, the

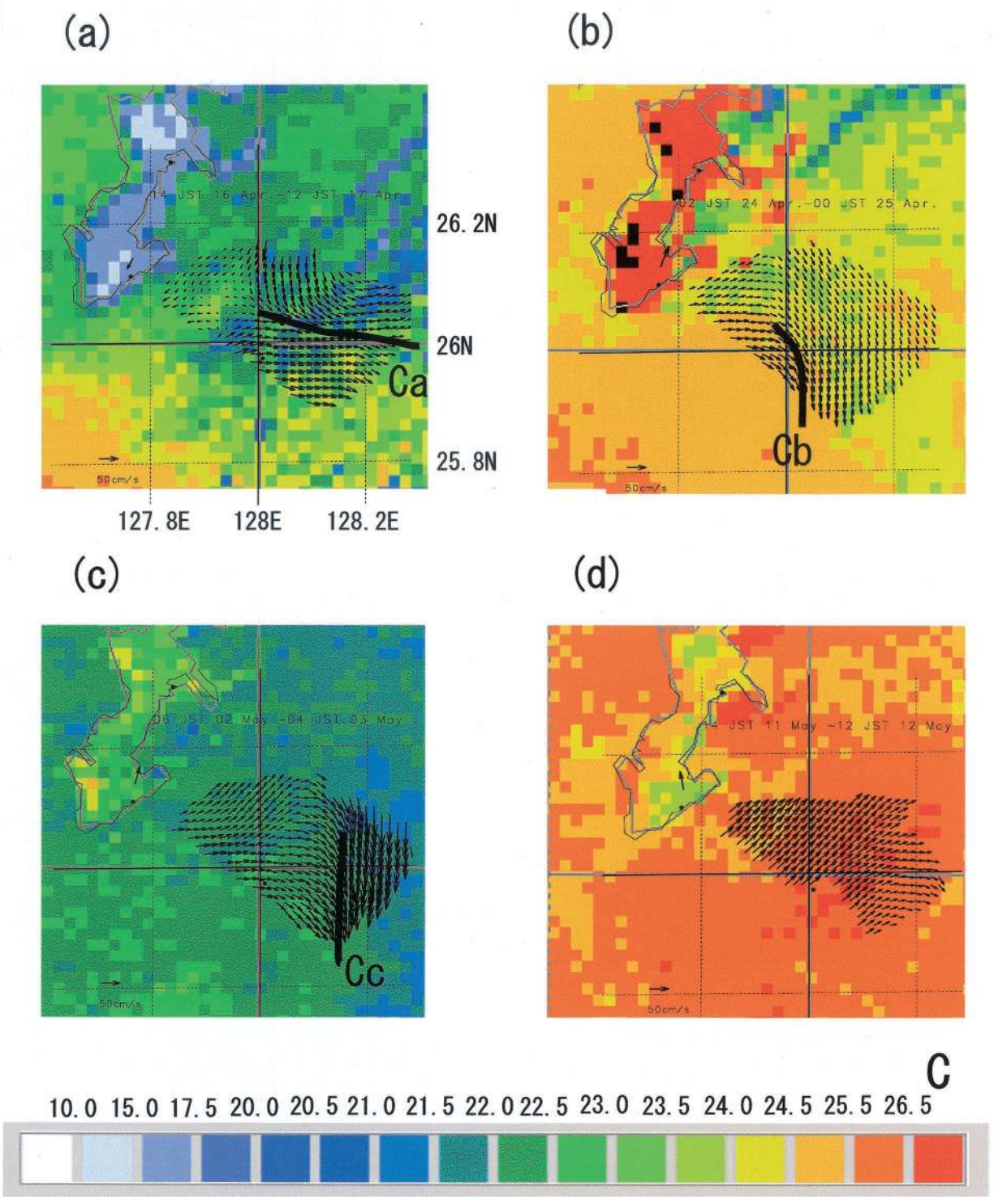

Plate 1. Twenty-four-hour averaged current vector maps overlapped with NOAA advanced very high resolution radiometer (AVHRR) imagery data. The time of NOAA/AVHRR imagery data and periods in which surface currents are averaged are (a) 0300 LT April 17, 1998 (NOAA/AVHRR imagery data), from 1400 LT April 16 to 1200 LT April 17, 1998 (surface currents); (b) 1500 LT April 24, 1998 (NOAA/AVHRR imagery data), from 0200 LT April 24 to 0000 LT April 25, 1998 (surface currents); (c) 1800 LT May 2, 1998 (NOAA/AVHRR imagery data), from 0600 LT May 2 to 0400 LT May 3, 1998 (surface currents); (d) 0300 LT May 12, 1998 (NOAA/AVHRR imagery data), and from 1400 LT May 11 to 1200 LT May 12, 1998 (surface currents).

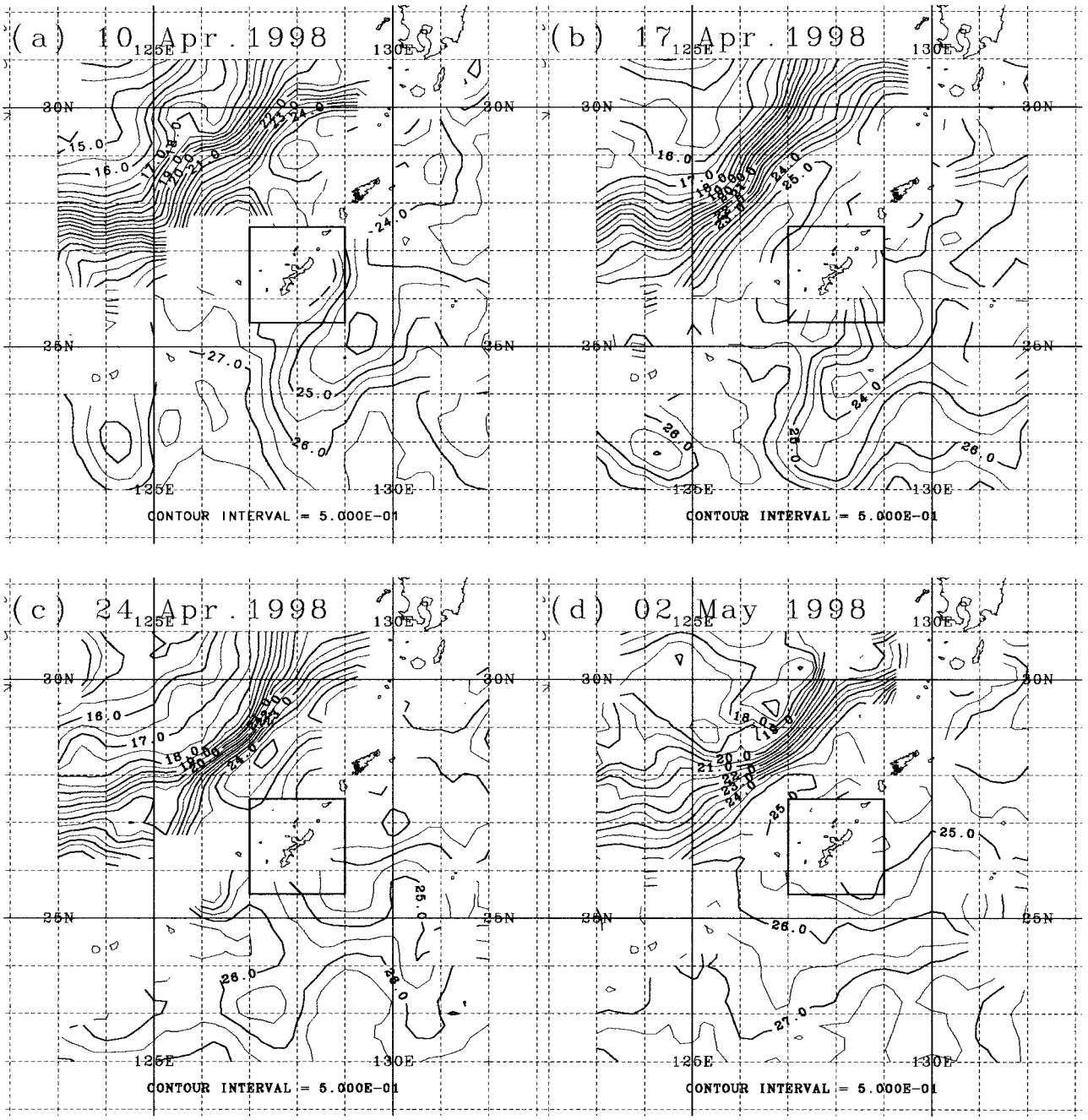

Figure 16. Examples of daily SST from TMI: (a) April 11, 1998, (b) April 17, 1998, (c) April 24, 1998, and (d) May 2, 1998. The box in each panel (127°E–129°E and 25.5°N–27.5°N) outlines the area of Figure 1 for reference.

convergence appears associated with a temperature front (Plate 1a). We can also see a less intense convergent zone near region Cb in Plate 1b, which is also associated with a temperature front, but the contrast in temperatures is not as clear as in Plate 1a. A convergent zone between southeastward and southward flows is also seen around Cc in Plate 1c coincident with a temperature front. On the other hand, we do not see a clear convergent zone in in Plate 1d, the time when water intruded northeastward.

5.2.2. Daily SST from TMI. Figure 16 shows examples of daily SST from the TMI. Figure 16a shows the SST distribution when the temperature abruptly rose at Payao (Figure 8c). (Note that this day (April 10, 1998) was before the HF ocean radars were operating.) We can see that warm water intruded east of Okinawa Island. The temperature front in Figure 16a is located around 27°N, 129°E. Figure 16b shows the SST distribution when strong convergence was observed by the HF ocean radars. We can see a temperature front in the vicinity of the HF ocean radar observation area. The front in Figure 16b is located farther south than the front in Figure 16a. In Figures 16c and 16d the front is not as clear as in Figure 16b, but there are no SST data from the TMI near the coast.

Considering the T/P altimetric data described in section 3.1 and TMI SST data, we conclude that strong convergences

observed by HF ocean radars were associated with fronts of warm (anticyclonic) or cold (cyclonic) eddies. When a front associated with a mesoscale eddy existed in the HF ocean radar observation area, it coincided with a convergent zone in the surface flow. The position of the front migrated southward and northward during the observation period.

6. Summary and Discussion

We investigated surface current variability east of Okinawa Island using in situ and remotely sensed data, especially from HF ocean radars. There have been few previous observational studies around this region. Most previous studies utilizing HF ocean radars were limited to continental shelves; however, in this study, most of the observation area was the open ocean. A pair of counterclockwise and clockwise mesoscale eddies existed in the region east of Okinawa Island during our observation period; the HF ocean radars observed between these mesoscale eddies.

We compared HF-ocean-radar-derived currents with in situ data and found reasonable agreement. This supported our analysis of ocean currents based on HF ocean radar data. We surmise that the reason for this good agreement is because winds were not so strong during the observation period (Figure 9) and the vertical variability associated with wind-driven currents as Ekman drift currents was not large. We also found reasonable agreement between daily-averaged buoy-measured temperatures and SST from TMI.

The mean current fields inferred from HF ocean radars were consistent with the altimetic data, which indicates that the current fields were affected by mesoscale eddies. Furthermore, the correlation map between land-based winds and surface currents suggested that the influence of mesoscale eddies increased in the deep ocean. The northeastward current associated with mesoscale eddy flow was accompanied by a rise in water temperature near the surface. Tidal analysis of the current data suggested that internal tides were dominant in the region.

A strong convergent zone was often detected. The value of the convergence was about 10×10^{-5} s^{-1} for daily-averaged currents. This convergent zone is apparently a different type from those in previous studies. It exists in the deep open ocean. From SST maps of NOAA/AVHRR data, and considering the T/P altimetric data and SST from TMI, we conclude that the convergent zones are ageostrophic currents associated with fronts of mesoscale eddies. Although a convergence zone associated with a front in a continental shelf or a continental shelf break has previously been detected by HF ocean radars, the strong convergence zone associated with a mesoscale eddy front has never been detected in detailed fashion. The front migrated and was often detected by HF ocean radars.

Although the observation area east of Okinawa Island is far from the Kuroshio, it might be affected by it. For example, in Figure 7b we can see Kuroshio countercurrents from isotherms at 27°–28°N, 127°–128°E to the south of the Kuroshio, and the Kuroshio countercurrents flowed southwestward. On the other hand, in Figures 7c–7e the temperature gradients in this region (27°–28°N, 127°–128°E) were weakened. The relationship between the Kuroshio and events east of Okinawa Island, for example, a convergent zone associated with a front and an intrusion of warm water east of Okinawa Island, will be the subject of future study.

We demonstrated that HF ocean radars are useful not only for physical oceanography but also for fishery research, because in the convergence region, nutrient salt is rich, so it is a good fishing area. The movement and fluctuation of the magnitude of the convergent zone should be investigated in the future.

Acknowledgments. We thank the anonymous reviewers and the editor (John Toole) for their insightful comments, which improved the manuscript. We acknowledge S. Kakuma, Okinawa Prefectural Fisheries Experiment Station, for providing data at Payao. We acknowledge the staff of the Geographical Survey Institute and Japan Meteorological Agency for providing the tidal and wind data, respectively. The T/P data were obtained from the NASA Physical Oceanography Distributed Active Archive Center at the Jet Propulsion Laboratory, California Institute of Technology, and were compiled by M. Koga, University of the Ryukyus. The NOAA/AVHRR data were supplied from western Japan satellite data workgroups. TMI SST data (version 2.0) were produced and supplied by the Earth Observation Research Center, National Space Development Agency of Japan (http://www.eorc.nasda.go.jp/TRMM/). The GFD-DENNOU Library (http://dennou.gaia.h.kyoto-u.ac.jp/arch/dcl/) was used in drawing the figures.

References

Barrick, D. E., Extraction of wave parameters from measured HF sea-echo Doppler spectra, *Radio Sci*., *12*, 415–424, 1977.

Barrick, D. E., M. W. Evans, and B. L. Weber, Ocean surface currents mapped by radar, *Science*, *198*, 138–144, 1977.

Benada, R., Merged GDR (TOPEX/POSEIDON) generation B users handbook, version 2.0, *Rep*. *JPLD-11007*, Jet Propul. Lab., Pasadena, Calif., 1997.

Chapman, R. D., L. K. Shay, H. C. Graber, J. B. Edson, A. Karachintsev, and C. L. Trump, On the accuracy of HF radar current measurements: Intercomparisons with ship-based sensors, *J. Geophys. Res*., *102*, 18,737–18,748, 1997.

Graber, H. C., B. K. Haus, R. D. Chapman, and L. K. Shay, HF radar comparisons with moored estimates of current speed and direction: Expected differences and implications, *J. Geophys. Res*., *102*, 18,749–18,766, 1997.

Hisaki, Y., Nonlinear inversion of the integral equation to estimate ocean wave spectra from HF radar, *Radio Sci*., *31*, 25–39, 1996.

Hisaki, Y., Correction of amplitudes of Bragg lines in the sea echo Doppler spectrum of an ocean radar, *J. Atmos. Oceanic Technol*., *16*, 1416–1433, 1999.

Hisaki, Y., and M. Tokuda, VHF and HF sea-echo Doppler spectrum for a finite illuminated area, *Radio Sci*., *36*, 425–440, 2001.

Marmorino, G., C. L. Trump, F. Askari, N. Allan, D. B. Trizna, and L. K. Shay, An occluded coastal oceanic front, *J. Geophys. Res*., *103*, 21,587–21,600, 1998.

Matthews, J. P., A. D. Fox, and D. Prandle, Radar observation of an along-front jet and transverse flow convergence associated with a North Sea front, *Cont. Shelf Res*., *13*, 109–130, 1993.

Paduan, J. D., and L. K. Rosenfeld, Remotely sensed surface currents in Monterey Bay from shore-based HF radar (Coastal Ocean Dynamics Application Radar), *J. Geophys. Res*., *101*, 20,669–20,686, 1996.

Shay, L. K., H. C. Graber, D. B. Ross, and R. D. Chapman, Mesoscale surface current structure detected by HF radar, *J. Atmos. Oceanic Technol*., *12*, 881–900, 1995.

Shay, L. K., S. J. Lentz, H. C. Graber, and B. K. Haus, Current structure variations detected by HF radar and vector measuring current meters, *J. Atmos. Oceanic Technol*., *15*, 237–256, 1998.

Shibata, A., K. Imaoka, M. Kachi, and H. Murakami, SST observation by TRMM microwave imager aboard tropical rainfall mission (in Japanese), *Umi Kenkyu*, *8*, 135–139, 1999.

Takeoka, H., Y. Tanaka, Y. Ohno, Y. Hisaki, A. Nadai, and H. Kuroiwa, Observation of the Kyucho in the Bungo Channel by HF radar, *J. Oceanogr*., *51*, 699–711, 1995.

Teague, C. C., Multifrequency HF radar observations of currents and current shears, *IEEE. J. Oceanic Eng*., *OE-11*, 258–269, 1986.

Weller, R. A., D. L. Rudnick, C. C. Eriksen, K. L. Polzin, N. S. Oakey, J. W. Toole, R. W. Schmitt, and R. T. Pollard, Forced ocean response during the frontal air-sea interaction experiment, *J. Geophys. Res*., *96*, 8611–8638, 1991.

Yang, Y., C-T. Liu, J.-H. Hu, and M. Koga, Taiwan Current (Kuroshio) and impinging eddies, *J. Oceanogr*., *55*, 609–617, 1999.

Yuan, Y., A. Kaneko, J. Su, X. Zhu, Y. Liu, N. Gohda, and H. Chen, The Kuroshio east of Taiwan and in the East China Sea and the currents east of Ryukyu Islands during early summer of 1996, *J. Oceanogr*., *54*, 217–226, 1998.

S. Fujii and K. Sato, Okinawa Radio Observatory, Communications Research Laboratory, 829-3, Daigusukubaru, Aza-Kuba, Nakagusukuson, Nakagami-gun, Okinawa 901-2401 Japan. (fujii@crl.go.jp; satoken@crl.go.jp)

W. Fujiie and T. Tokeshi, Interdisciplinary Graduate School of Engineering Sciences, Kyushu University, 6-1 Kasuga-Kouen, Kasuga-shi, Fukuoka 816-8580 Japan. (wataru@riam.kyushu-u.ac.jp)

Y. Hisaki, Department of Physics and Earth Sciences, Faculty of Science, University of the Ryukyus 1 Aza-Senbaru, Nishihara-cho, Nakagami-gun, Okinawa 903-0213 Japan. (hisaki@sci.u-ryukyu.ac.jp)

(Received January 2, 2001; revised July 10, 2001;
accepted July 10, 2001.)